ARTICLE

Fast and Versatile Electrodeposition of Vertically Aligned Layered Rare-Earth Hydroxide Nanosheets for Multicolour Luminescence and Oil/Water Separation †

Received 00th January 20xx,
Accepted 00th January 20xx

DOI: 10.1039/x0xx00000x

Xiaoli Wu[a,b,c], Yongping Guo[a,b], Ji-Guang Li[d*] and Yuanli Liu[a,b,c*]

The construction of multifunctional films using layered rare-earth hydroxide (LREH) nanosheets as building blocks is a subject of topical interest, where the traditional technique involves four major steps: bulk crystal synthesis, intercalation of long-chain organic anions, exfoliation of the bulk crystals into nanosheets, and layer-by-layer deposition of the nanosheets into a film. We originally established herein an electrodeposition technique that allows for one-step film construction in only 10 minutes and for a wide range of RE elements (RE=La-Ho lanthanides and Y, excluding Ce). Distinctly different from the [001] oriented LREH films made via the traditional technique, the LREH nanosheets were significantly aligned vertically to the substrate surface and showed super-hydrophobicity. With the LYH for example, high efficiency of oil/water separation was achieved with the film grown on a nickel mesh, and the similarly structured oxide films transformed from the Eu^{3+}, Tb^{3+} and Eu^{3+}/Tb^{3+} doped LYH films, grown on ITO glass, showed multi-color luminescence (green, orange, and red), long luminescence lifetime and high quantum efficiency. This study provided a new concept for the design and fabrication of multifunctional LREH materials that might help broaden the application of LREH.

1 Introduction

Layered rare-earth hydroxides (LREHs), with a general composition of $RE_2(OH)_5A{\cdot}nH_2O$ [RE = rare-earth (RE) ions, A = exchangeable anions], are an emerging layered compounds which was first reported in 2006.[1] The LREHs structurally similar to LDHs, consisting of alternating positively charged host layers of $[RE_2(OH)_5{\cdot}nH_2O]^+$ (edge sharing of $[Ln(OH)_7H_2O]$ and $[Ln(OH)_8H_2O]$ polyhedrons) and exchangeable anions (such as NO_3^-) along the *c*-axis, as shown in Fig. 1a.[2-3] During the past several years, LREHs have attracted widespread attention owing to the diverse physicochemical properties of the RE elements and the rich interlayer chemistry of the layered compounds. Studies on this group of new layered compounds have largely focused on the interlayer anion exchange,[2-6] catalytic function of intercalated products,[1,6-7] photoluminescence,[2-4,8-9] enhancement of luminescence via intercalation of organic[10-12] or inorganic sensitizers,[4,13] derivation of oxide phosphors via calcination[8,14-15] and fabrication of highly transparent ceramic with LREHs as a new type of precursor.[16-18] Also, the self-assembly of functional films is one of the most attractive aspects of LREHs.[19-21] However, the plate-like LREH crystals obtained by well-established methods including hydrothermal route[5,8-9] and homogeneous precipitation via refluxing[2] are typically tens to hundreds of nanometres in thickness and several microns in lateral dimension, which are not suitable for preparing transparent luminescent films directly. In this regard, delamination of thick LREH crystals into ultrathin nanosheets is indispensable, which can be achieved via anion exchange of the interlayer NO_3^- with significantly long-chain anions such as $C_{12}H_{25}OSO_3^-$ (DS-)[17-18,22] or $C_{17}H_{33}COO^-$,[23] followed by sufficient mechanical agitation in formamide. Finally, the resulting ultrathin nanosheets as building blocks are used for the construction of functional films via spin-coating,[17-18,23] simple dipping,[20] layer by-layer deposition[21] and solvent casting.[12] It is thus clear that the traditional preparation of the LREH film as shown in Fig. 1a needs four steps: synthesis of LREH crystals, intercalation of long-chain organic anions, exfoliation of LREH crystals into ultrathin nanosheets, and formation of the film using exfoliated nanosheets. The LREH nanosheets tend to orient themselves parallel to the substrate surface to form a highly [00l]-oriented LREH film[17-24] because of the significant morphological anisotropy. Despite these successes, the whole process for the formation of the LREH film is laborious and time-consuming. Moreover, the intercalation of long-chain organic anions is difficult due to the strong interlayer electrostatic interaction, high content of charge compensating ionic species sandwiched between the layers, and/or strong hydrogen bonding,[3-4] and it easily results in incomplete exfoliation and fragmentation of nanosheets.

[a] College of Materials Science and Engineering, Guilin University of Technology, Guilin 541004, P. R. China
[b] Guangxi Key Laboratory of Optical and Electronic Materials and Devices, Guilin University of Technology, Guilin 541004, P. R. China
[c] Collaborative Innovation Center for Exploration of Hidden Nonferrous Metal Deposits and Development of New Materials in Guangxi; Guilin University of Technology, Guilin 541004, China
[d] Research Center for Electronic and Optical materials, National Institute for Materials Science, Namiki 1-1, Tsukuba, Ibaraki 305-0044, Japan
E-mail: lyuanli@glut.edu.cn (Y. L. Liu)
Electronic Supplementary Information (ESI) available: Experimental, Fig. S1–S8.
See DOI: 10.1039/x0xx00000x

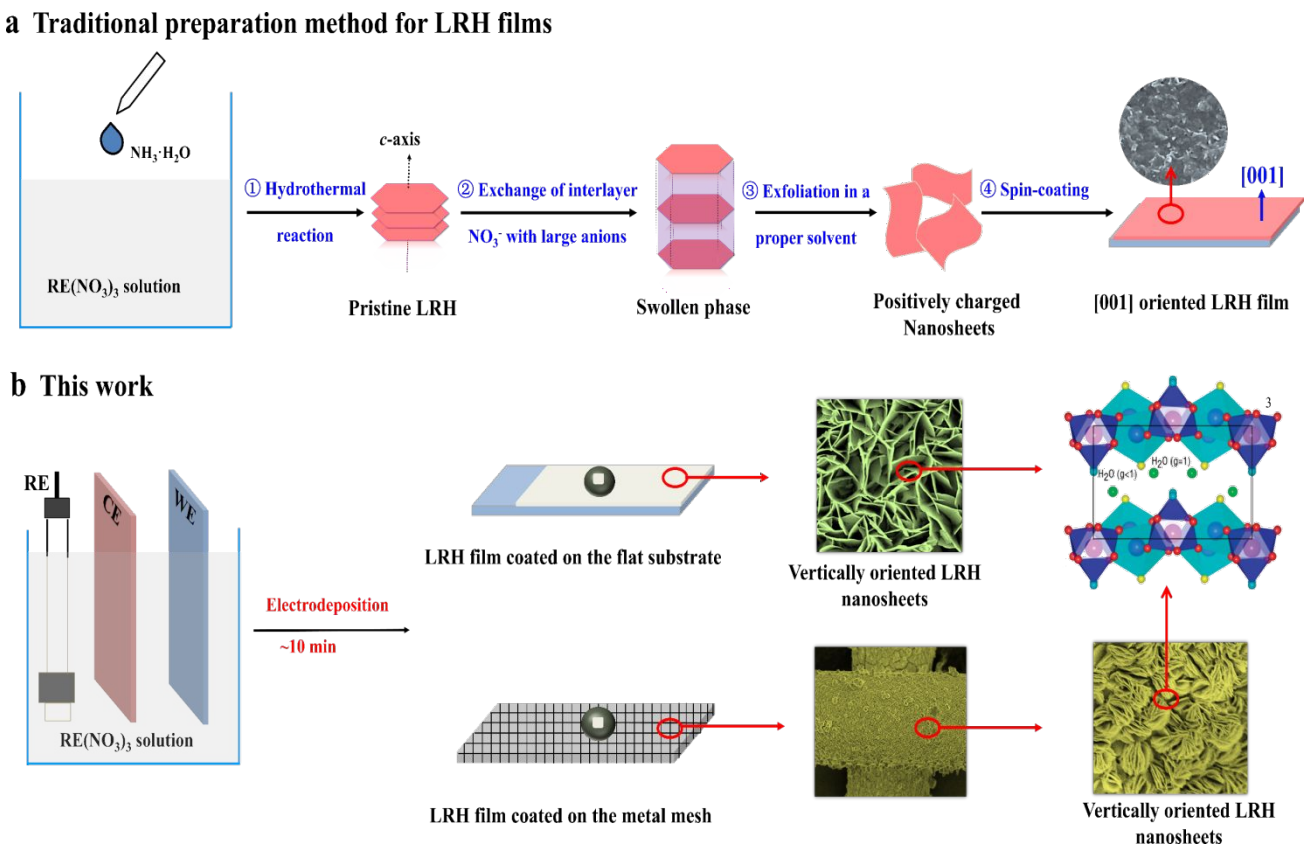

Fig. 1 Schematic of the traditional preparation method for LREH films (a) and the electrodeposition preparation in this work (b).

In this study, we proposed an efficient method to prepare LREH films on flat substrate and metal mesh within 10 min (Fig. 1b). The obtained LREH nanosheets were found to be significantly aligned vertically to the substrate surface, which endows the film with super-hydrophobicity. The high efficiency of oil/water separation was thus achieved with the LYH film grown on a nickel mesh. In addition, Y_2O_3:RE films with multicolour luminescence and long luminescence lifetime were transformed from the LYH films based on the quasi-topotactic conversion.

2. Experimental

2.1 Materials

The starting rare-earth sources are $RE(NO_3)_3{\cdot}6H_2O$ (99% pure, Ln = La, Pr, Nd, Gd, and Tb), $RE(NO_3)_3{\cdot}6H_2O$ (99.9% pure, Ln = Sm, Eu, and Dy), $Ho(NO_3)_3{\cdot}5H_2O$ (99.9% pure) and $Y(NO_3)_3{\cdot}6H_2O$ (99.5% pure), which were purchased from Shanghai Macklin Biochemical Co., Ltd. The indium tin oxide (ITO) glass (Square resistance: ≤5 Ω) were obtained from Xiang Cheng Technology Ltd. China. The platinum electrode and Ag/AgCl/saturated KCl electrode were purchased from Tianjin Ida Technology Co. Ltd., China. Nickel mesh was purchased from Hebei Yuqian Metal Materials Co. Ltd., China.

2.2 Synthesis

For the synthesis of $Y_2(OH)_5NO_3{\cdot}nH_2O$ (LYH) film, $Y(NO_3)_3$ was firstly dissolved in deionized water to make 0.1 M $Y(NO_3)_3$ solution, which was used as electrolyte solution. Electrodeposition was carried out in a standard three-electrode cell at room temperature with a proper applied potential for several minutes (5-10 min). The three electrodes are connected to electrochemical workstation (IviumStat.h, Ivium, Netherland). Then, the obtained films were cleaned with deionized water and dried in air at 60 °C for 10 min. Also, the technique was extended to the synthesis of $RE_2(OH)_5NO_3{\cdot}nH_2O$ (RE = La, Pr, Nd, Sm, Eu, Gd, Tb, Dy and Ho) films. For the synthesis of photoluminescent Y_2O_3:0.005Eu, Y_2O_3:0.03Tb and Y_2O_3:0.005Eu0.03Tb films, different amounts of $Y(NO_3)_3$, $Eu(NO_3)_3$ and $Tb(NO_3)_3$ were firstly dissolved in deionized water to make 0.1 M $Y(NO_3)_3$ solution, 0.01 M $Eu(NO_3)_3$ solution and 0.01 M $Tb(NO_3)_3$ solution, respectively. These solutions were mixed according to the molar ratio of $n_Y : n_{Eu}$=0.995:0.005, $n_Y : n_{Tb}$=0.97:0.03, $n_Y : n_{Tb} : n_{Eu}$ =0.965:0.03:0.005, and the obtained solutions were used as electrolyte solution. The activator doped LYH films were deposited on the ITO-coated substrates at room temperature, and then annealed at 600 °C in the nitrogen atmosphere for 2 h. However, using the same process conditions as mentioned above to deposit LYH film on nickel mesh result in poor coverage. Therefore, LYH film was prepared on the nickel mesh using pulse electrodeposition. The potential was set to -1.15 V, the pulse width (T_{on}) and interval (T_{off}) were both set to 0.05 s, and the cycle number was set to 120.

2.3 Characterization

Phase identification of films was performed via X-ray diffraction (XRD, X'Pert PRO, PANalytical B.V.) operated at 40kV/40mA nickel filtered using Cu-kα radiation (λ=0.15406 nm). The morphology and

microstructure of films were detected with a field emission scanning electron microcopy (FE-SEM, JSM6380-LV, JEOL) and transmission electron microscopy (TEM, Model JEM-2000FX, JEOL). Fourier transform infrared spectroscopy (FT-IR, Model Spectrum RXI, Perkin-Elmer, Shelton, Connecticut) was conducted by the standard KBr method. The chemical composition of the compound was determined by elemental analysis, with the Y^{3+} content analyzed by the inductively coupled plasma (ICP) spectrophotometric method (Model 7700s, Agilent Technologies Inc., USA) and the nitrogen and carbon contents assayed with a Flash Smart analyzer (Thermo Fisher Scientific Inc., Italy). The static contact angles of water were measured using a contact angle goniometer (SL200KS, USA) at room temperature. The deviation/error of the contact angle measuring instrument we used is ±1°. Photoluminescence/photoluminescence excitation (PL/PLE) and fluorescence decay were measured at room temperature using an FP-8500 fluorescence spectrophotometer (JASCO, Tokyo), with a 150-W Xe-lamp as the excitation source. The internal quantum efficiency (η_{in}, the total number of emitted photons divided by the number of excitation photons absorbed by the sample) of the oxides are derived from the following equation (1) using the built-in analysis software:

$$\varepsilon_{in} = \frac{\int \lambda P(\lambda) d\lambda}{\int \lambda [E(\lambda) - R(\lambda)] d\lambda} \quad (1)$$

where $E(\lambda)/hv$, $R(\lambda)/hv$, and $P(\lambda)/hv$ are the number of photons in the excitation, reflectance, and emission spectra of the samples, respectively.

3. Results and discussion

Taking the preparation of the $Y_2(OH)_5NO_3{\cdot}nH_2O$ (LYH) film as an example, as illustrated in Fig. 2, the experiment was conducted in a standard three-electrode system, with the $Y(NO_3)_3$ solution as an electrolyte, Ag/AgCl/saturated KCl as the reference electrode, and Pt net and ITO glass as the counter electrode and working electrode, respectively. According to the phase selection mechanism of LREH, the nucleation and growth of LYH are mainly related to the pH of the solution.[4,25] In this new method, electrochemical reduction first occurs at the cathode and provides OH^- on the surface of ITO glass, which increases the local pH and achieves the growth conditions of LREH. Then, the surrounded Y^{3+}, NO_3^- and H_2O diffuse to the cathode and combine with OH^- to form $Y_2(OH)_5NO_3{\cdot}nH_2O$ phase and deposit on the ITO surface. The experimental results indicate that the effective voltage to form the LYH phase at room temperature is from -0.90 to -1.3 V (*vs*. Ag/AgCl/saturated KCl) (Fig. S1). Only a small amount of sediment or even no deposit sediment is found on the cathode when the working voltage is lower than -0.9 V. However, the obtained film turns to black due to overvoltage when the working voltage is higher than -1.3 V. With this strategy, a thin white film can be obviously observed on the cathode surface in as fast as 5 min. This electrodeposition method can also deposit films on the metal meshes, such as nickel mesh. As shown in Fig. 3(a)-(b), the XRD patterns of the films deposited on the different substrates agree with the LYH compound,[2-5] where the (00*l*) diffractions are the characteristic of the layered compounds, while the (220) diffraction is known to originate from the $[RE_2(OH)_5(H_2O)_n]^+$ host layer. The strong and sharp (220) diffraction indicates that the hydroxide layers are well crystallized, as confirmed by TEM analysis (Fig. S2). FT-IR spectra of the films (Fig. 3c) further confirmed the existence of all the functional groups of the LYH structure, including the absorption of hydroxyls centered at 3580 cm^{-1}, water molecules at 3380 cm^{-1} (O-H stretching vibrations v_1 and v_3) and 1645 cm^{-1} (H-O-H bending mode v_2), uncoordinated nitrate anions at 1384 cm^{-1}, and bending/stretching vibration of Y-O at 635 cm^{-1}.[4,8-9,14] Chemical analysis found 49.5 wt.% of Y, 3.85 wt.% of N, and 0.48 wt.% of C for the electrodeposited film after drying, corresponding to Y/N/C and Y/N molar rations of 2/0.99/0.13 and 2/0.99 (close to 2/1), respectively. According to the literature, all the C comes from CO_3^{2-}, which can be ascribed to CO_2 from the atmosphere, as LREHs have a strong affinity to CO_2 and a few amounts of CO_3^{2-} anions is thought to simply replace hydroxyls.[2,4] The results thus suggest that the prescribed atomic ratio has essentially been kept to the obtained product and LYH film has been formed. The field emission–scanning electron microscope (FE-SEM) (Fig. 3d) morphology of the LYH film deposited on the ITO substrate is significantly different from that of the highly [001]-oriented LYH film (Fig. S3) prepared using the "four-step" method, in which LYH nanosheets tend to grow in a direction perpendicular to the substrate rather than parallel to the substrate. In general, the precipitation of solid crystals from a solution needs to undergo nucleation and crystal growth. As the host layer of LREH is a close-packed low-energy plane, the crystal preferentially grows along the *ab* plane, leading to the frequently observed in a two-dimensional morphology. In this electrodeposition method, a large amount of OH^- are produced simultaneously on the surface of the substrate, and then initial heterogeneous nucleation occurs on the substrate. Due to the space constraints, LREH nanosheets tend to grow in a direction perpendicular to the substrate. This new synthesis technique clearly endows the LYH film with a highly rough surface, and this inspired us to think about the super-hydrophobicity of the electrodeposited LYH film. From the inset of the Fig. 3d, one sees that the LYH film exhibits obvious super-hydrophobicity phenomenon as we expected. Metal mesh, as pore-structured semipermeable barriers made of connected metal strands, are frequently used for oil/water separation after surface roughening.[26-28] As show in Fig. S4, the original nickel mesh substrate is knitted by Nickle wires, and it exhibits a relative lower water contact angle. After adopting our electrodeposition-based route, one sees that the LYH layer uniformly and completely covered the nickel mesh (Fig. 3e). High-magnification SEM image (see the insets in Fig. 3e) of the LYH-coated nickel mesh shows that numerous nanosheets vertically stand on the surface of the nickel mesh, still maintaining a high-roughness surface. As such, the water contact angle of the mesh increases obviously (see the inset of Fig. 3e). Interestingly, it is found that the nanosheets grown on the nickel mesh are denser using the pulse electrodeposition under the same working voltage of -1.15 V. It is known that a pulse cycle T is divided into two parts: the conduction time (T_{on}) and the turn off time (T_{off}). T_{on} represents the deposition process of ions, while T_{off} represents the time for ion replenishment.

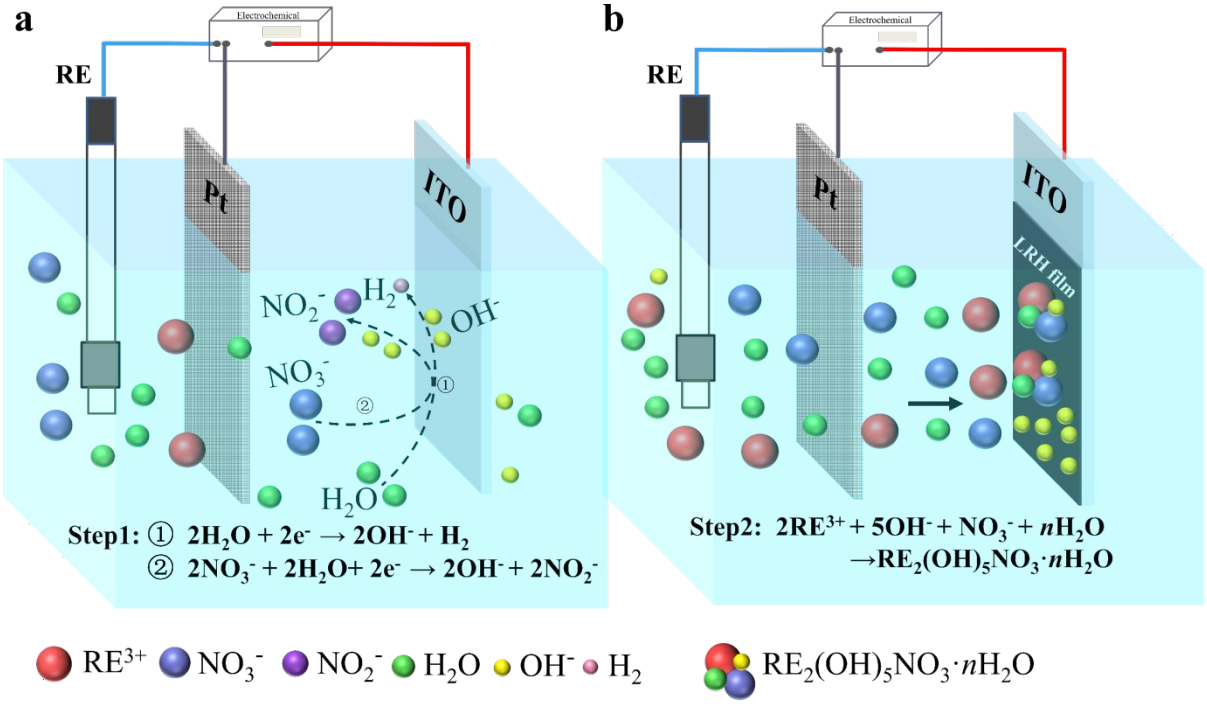

Fig. 2 Schematic illustration of the fabrication processes, including electrochemical reduction (a) and the formation of $Y_2(OH)_5NO_3 \cdot nH_2O$ film on the ITO glass (b).

During the constant voltage electrodeposition, the deposited ions near the cathode are continuously deposited, resulting in concentration polarization. In the process of pulse electrodeposition, the concentration of deposited ions around the cathode can be supplemented due to the existence of turn off time. The above analysis shows that pulse electrodeposition not only reduces the concentration difference polarization of the cathode, but also increases the instantaneous current density. This causes the ions are deposited at extremely high overpotentials, which promotes nucleation rate greater than the growth rate.[29] Therefore, LYH film prepared by pulse electrodeposition method has a tighter arrangement of nanosheets and relative smaller nanosheets. The functionalized metal meshes was fixed using a connector, and two ends of the connector were attached with two glass tubes to make a simple oil-water separation device (Fig. 3f). The ESI Video S1 presented the oil/water separation process in which a mixture of water (dyed blue) and petroleum ether (dyed red) was poured into the upper tube, and petroleum ether (dyed red) rapidly passed through the meshes with the driving force of gravity, indicating the high efficiency of oil/water separation. To further investigate the influence of various variables of the electrodeposition technique on the growth of LREH films, LYH film was selected as a representative example and deposited it on the ITO glass under different conditions (operating voltage and temperature). Since the tolerance temperature of the reference electrode being 80 °C, all of the comparison experiments were conducted under the conditions below 80 °C. According to the crystallization habit of LREH,[3-4] the growth of crystals along the *c*-axis direction requires higher activation energy compared to the growth in the *ab* direction. According to the literature,[7-9] the increase in reaction temperature can provide sufficient energy to promote the crystal growth along both the *ab* direction and *c*-axis direction. As seen in Fig. S5a-c, an increase in reaction temperature thus causes the LYH sheets to become larger and thicker. While the increase in working voltage leads to an increase in current density, resulting in an increase in nucleation rate. Due to the increase in the instantaneous nucleation amount on the surface of ITO glass, LYH sheets are stacked more tightly together. Fig. S 5d-f confirms this viewpoint well.

In addition to the facile preparation, this electrodeposition technique developed for the LYH film was also successfully applied to a wide range of lanthanides, including La, Pr, Nd, Sm, Eu, Gd, Tb, Dy and Ho. By analysing the results of XRD and SEM, it was found that the "lanthanide contraction" has a significant effect on the crystal structure and micromorphology of the LREH. As shown in Fig. 3g, the (220) diffraction tends to shift to the high-angle side while the (002) diffraction to the low-angle side with the decrease of ionic radius of RE^{3+}, indicating that the "lanthanide contraction" leads to a corresponding gradual change in the structure of the host layer (*ab*-plane) and the interlayer spacing. According to the structure of LREH crystal, the dimensions of the *ab*-plane is related to the metal-to-metal distance,[2-4,30] a gradual decrease in the radius of the RE^{3+} had thus contribute to the shrink of the *ab*-plane (the decrease of the d_{220}). The interlayer spacing (d_{002}) gradually increases with the decrease of RE^{3+}, and the same trend of change was found in the previous reports.[2-4,30] It is noticed that the d_{002} in this work is in general agreement with the value (~8.3–8.9 Å) for the low hydration LREH phase (LH-LREH).[2-4] Due to the fact that the preparation and storage of LREH film in this work were carried out in an environment without humidity control, and the nanosheets of LREH greatly enhance the exposure of the ultra-thin hydroxide main layer, making

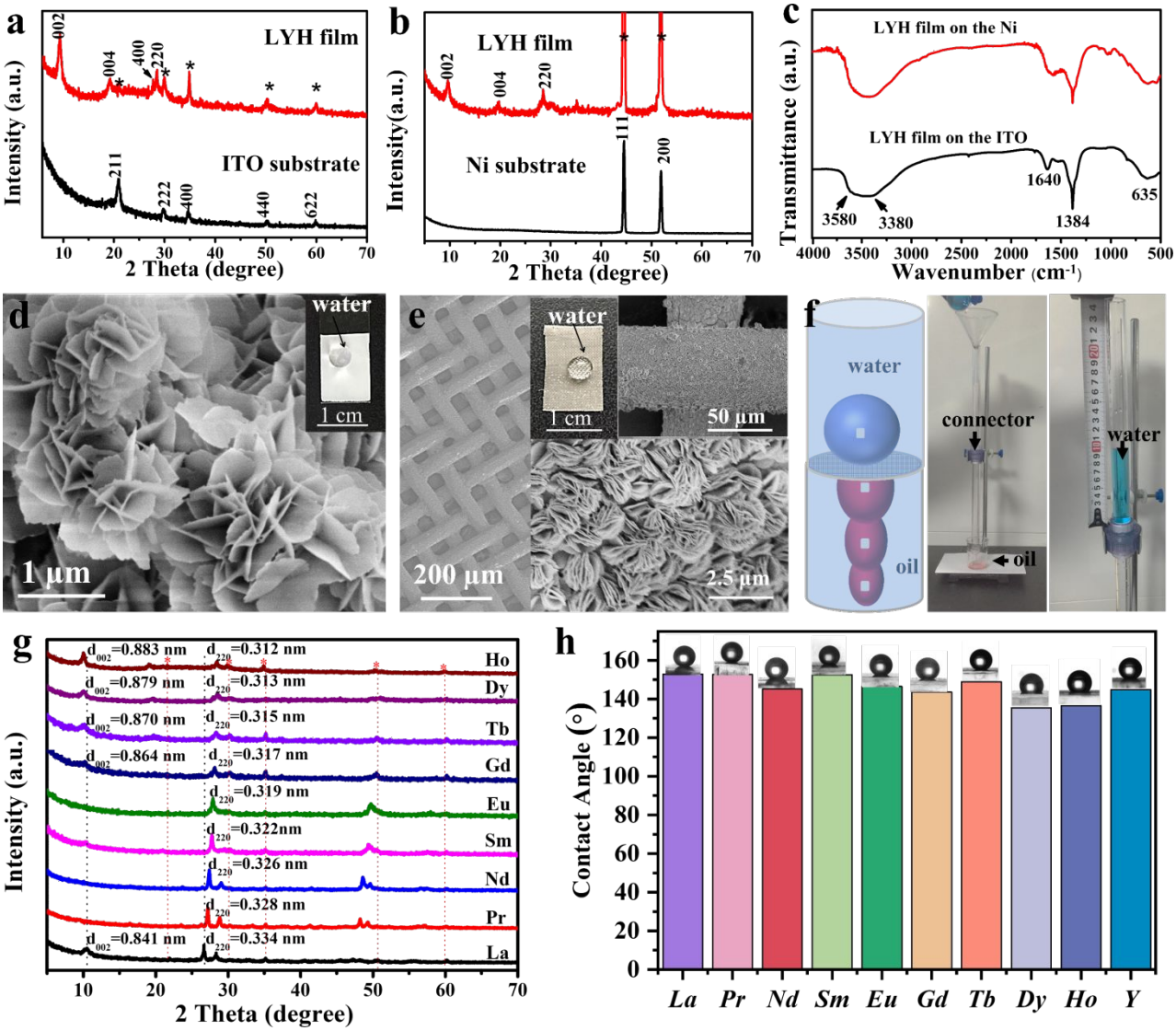

Fig. 3 XRD patterns (a-b), FT-IR spectra (c), FE-SEM morphologies (d-e) of the LYH films deposited on the different substrates; schematic and physical diagram of oil/water separation using LYH-coated nickel mesh (f); XRD patterns (g) and the corresponding water contact angles on the $RE_2(OH)_5NO_3{\cdot}nH_2O$ (RE = La, Pr, Nd, Sm, Eu, Gd, Tb, Dy and Ho) films (h). The insets in (d) and (e) display the corresponding physical images of water droplets attached to the surface of LYH films on the ITO glass and Nickle mesh, respectively.

it easier to form the LH-LREH phase. Our previous work[4] demonstrated that the interlayer distance for the LH-LREH is related to the spatial orientation of NO_3^- located in the hydroxide layers. As is known, a NO_3^- assumes a trigonal shape, and its spatial orientation is decided by the electrostatic interactions from the neighboring $[RE_2(OH)_5(H_2O)_n]^+$ host layers. The orientation of NO_3^- in the interlayer is expected to be more perpendicular (less parallel) to the hydroxide layer as the electrostatic attraction increases. It was found in previous works that the charge density of the hydroxide layer increases with a shrink in area of the *ab* plane (a decrease of RE^{3+} size)[31] and thus enhances the electrostatic attraction towards NO_3^-, which resulted in a gradually enlarged d_{002}. Such phenomenon is supported in the interlayer of cation-type layered compounds, where alkylammonium ions lie flat at relatively low charge density of the host layer and exhibit paraffin-type arrangements at high layer charge densities.[32] However, the intensities of (002) diffractions for LREH films are significantly weak for a larger ionic radius of RE^{3+} (RE= Pr^{3+}, Nd^{3+}, Sm^{3+}, Eu^{3+}, and Gd^{3+}), which can be attributed to a significantly preferred orientation of the LREH nanosheets. As shown in Fig. S6, the LREH nanosheets with a larger ionic radius of RE^{3+} are preferably oriented in a direction perpendicular to the surface of the substrate, while the enlarged SEM images of the LREH films with smaller RE^{3+} (Tb^{3+}, Dy^{3+}, and Ho^{3+}) show that some of the nanosheets tend to be parallel to the substrate. Such a morphology change has an impact on the hydrophobicity of the LREH films. As shown in Fig. 3h, the LREH films for smaller RE^{3+} (especially for Dy^{3+}) exhibits smaller contact angles, which is attributed to that more hydroxyls as hydrophilic group are exposed on the film surface. Another obvious phenomenon of "lanthanide contraction" is that the average size of LREH nanosheets decreases with a contraction of the Ln^{3+} radius, and they become much thinner. This may be attributed to an enhanced nucleation versus crystal growth upon the enhancement of

hydrolysis for the smaller RE^{3+}.[4,33] Unfortunately, for further smaller Er^{3+}-Lu^{3+}, no stable sediments were found on the ITO surface owing to the unfavorable more rapid kinetics of hydrolysis and precipitation. For larger Ce^{3+}, a plate-like CeO_2 film was obtained due to the facile oxidation of Ce^{3+} to Ce^{4+} (Fig. S7).

The photoluminescence study found that LEuH and LTbH exhibit the characteristic red and green emissions of Eu^{3+} and Tb^{3+}, respectively, which is of great interest to optical devices (Fig. S8). However, water molecules and hydroxyls are directly coordinated to the RE centers, which imposes a drastic quenching effect on the emissions of RE^{3+}, and thus leads to the emissions are far from industrial requirements. To improve the photoluminescence, removing the quenching groups via heat treatment is the most used optimization strategy.[14-16,19-21] According to the TG curve of LYH the film (Fig. 4a), the final decomposition temperature to form oxide occurred at 540 °C, which is close to the LYH powder form.[8] The XRD pattern of the film with heat treatment at 600 °C for 2 h reveals that all the diffraction peaks can be well indexed to the cubic Y_2O_3 (JPCDS No. 43-1036). Interestingly, the conversion from LYH to Y_2O_3 is a quasi-topotactic one due to a close metal arrangement between the (00*l*) lattice plane of the LYH and (111) plane of annealed oxide crystals.[19] The obtained Y_2O_3 film thus has well inherited the morphology of the precursor LYH film, which maintained a rough surface and super-hydrophobicity (Fig. 4c). As shown in Fig. 4d, the excitation spectrum of the $(Y_{0.995}Eu_{0.005})_2O_3$ film has one strong and broad charge transfer band (CTB) at ~240 nm, which could be assigned to the electron transfer from the 2p orbital of O^{2-} to the 4f orbital of Eu^{3+}. The film was excited with the peak wavelength of the CTB, and the oxide film exhibits the typical emissions of Eu^{3+}, with the transition of $^5D_0$-$^7F_2$ being the dominant one, as widely observed for Eu^{3+}-doped Y_2O_3 red phosphors. The emission spectrum of the $(Y_{0.97}Tb_{0.03})_2O_3$ film (Fig. 4e) measured at an excitation wavelength of

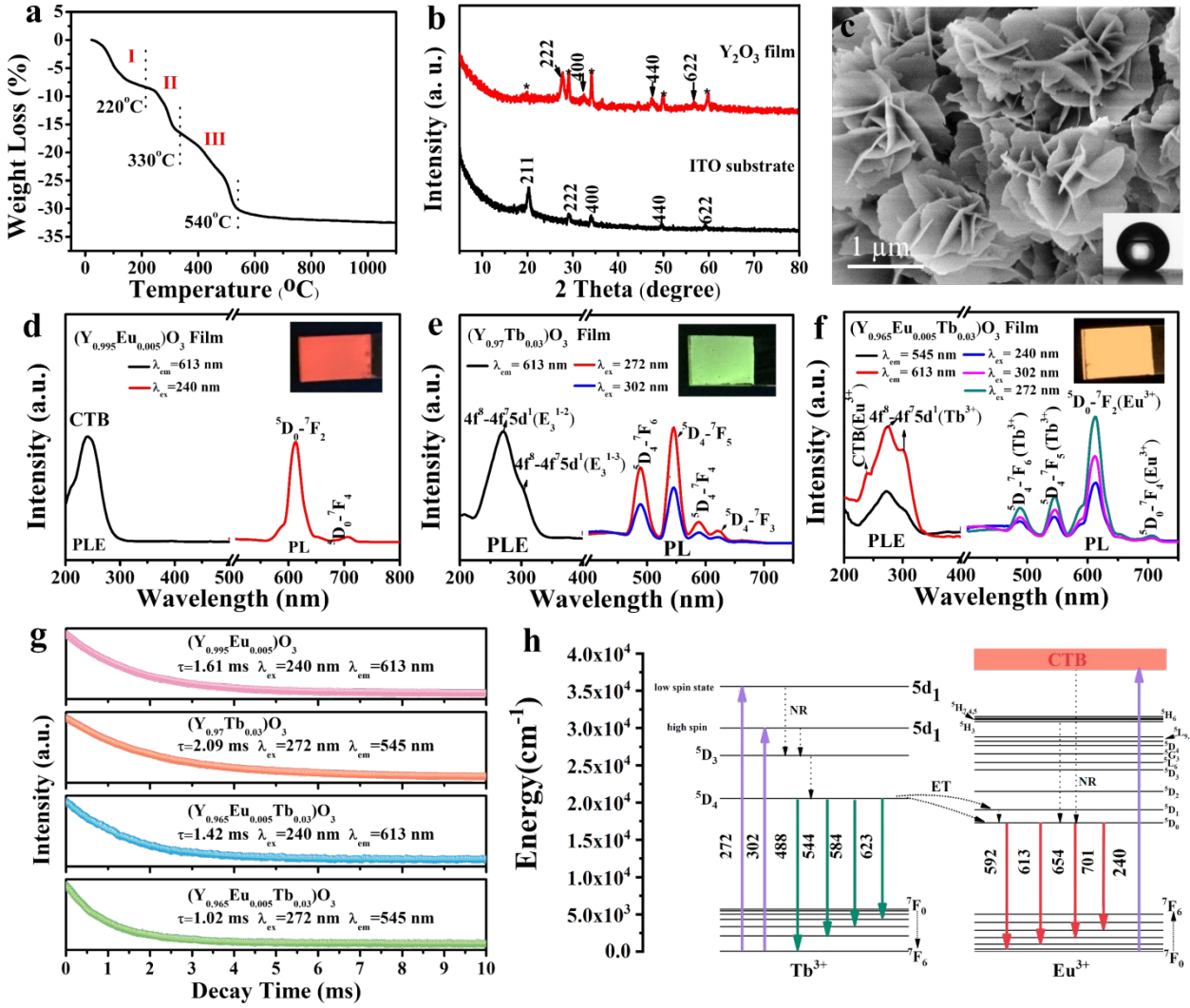

Fig. 4 TG curve (a), XRD pattern (b) and SEM morphology (c) of the cubic Y_2O_3 film; the PL/PLE spectra of the $(Y_{0.995}Eu_{0.005})_2O_3$ film (d), $(Y_{0.97}Tb_{0.03})_2O_3$ film (e), and $(Y_{0.965}Eu_{0.005}Tb_{0.03})_2O_3$ film (f); luminescence decay behaviour of the oxide films for the 545 nm emission and 613 nm emission, respectively (g); energy level scheme for energy transfer process among $(Y_{0.965}Eu_{0.005}Tb_{0.03})_2O_3$ films (h). The inset of (c) is the physical image of water droplets attached to the surface, and the insets of (d-e) show luminescence of the corresponding oxides under 254 nm excitation from a hand-held UV lamp.

272 nm and 302 nm ($4f^8$-$4f^75d^1$ transitions of Tb^{3+}), displays typical transitions of Tb^{3+} from the $^5D_4$ excited state to the ^7F_J (J = 6, 5, 4, 3) emission state. For the ternary $(Y_{0.965}Eu_{0.005}Tb_{0.03})_2O_3$ film (Fig. 4f), monitoring the 545 nm emission of Tb^{3+} yielded a PLE spectrum almost identical to that of the $(Y_{0.97}Tb_{0.03})_2O_3$ film (black line), while monitoring the 613 nm emission of Eu^{3+} produced both the f-d transition bands of Tb^{3+} and the CTB of Eu^{3+} (red line). This provides evidence of an efficient energy transfer from Tb^{3+} to Eu^{3+}. The emission decay curves of Tb^{3+} ($^5D_4$-$^7F_5$ line, 545 nm) of the oxide films are displayed in Fig. 4g. The decay curves fit well with a single exponential equ. (1),

$$I = A\exp(-t/\tau) + B \quad (1)$$

where τ is the fluorescence lifetime, I is the relative intensity, t is the decay time, and *A* and *B* are the fitting constants.[34,35] It can be seen that the oxides exhibit long luminescence lifetimes of Eu^{3+} and Tb^{3+}. Under 272 nm excitation, the decay times of Tb^{3+} ($^5D_4$-$^7F_5$ line, 545 nm) are 2.09 ms for the sample $(Y_{0.97}Tb_{0.03})_2O_3$ film, 1.02 ms for the sample $(Y_{0.965}Eu_{0.005}Tb_{0.03})_2O_3$ film, respectively. This result also verifies the energy transfer from doner Tb^{3+} to acceptor Eu^{3+}, and the energy transfer efficiency can further be determined by the Equation (2),

$$\eta = 1 - \tau/\tau_0 \quad (2)$$

where τ_0 and τ are the lifetime of the Tb^{3+} (donor) without and with Eu^{3+} (acceptor), respectively.[36] According to the formular (2), the energy transfer efficiency is 51%. As shown in Fig. 4h, the whole excitation and emission process of $(Y_{0.965}Eu_{0.005}Tb_{0.03})_2O_3$ film contains the following major steps. Under UV excitation, electrons of Tb^{3+} and Eu^{3+} can be excited to the 5d state and CT band, respectively. For Eu^{3+}, the higher excited state can be non-radiatively relaxed to the $^5D_0$ level, the oxide film displays the typical $^5D_0$ - ^7F_J (J= 1 to 4) transitions of Eu^{3+} at 592, 613, 654 and 701 nm, respectively. For Tb^{3+}, the excited electrons relax to the lowest excited state $^5D_4$ through multiphonon relaxation then either return to the ground state to produce the emissions ($^5D_4$ - $^7F_{6,5,4,3}$) or transfer their excitation energy to Eu^{3+} rapidly *via* non-radiative transitions to the $^5D_1$ and $^5D_0$ states. Subsequently, a non-radiative energy transfer occurs from $^5D_1$ to $^5D_0$ in Eu^{3+}, enhancing the characteristic $^5D_0$-$^7F_2$ emission of Eu^{3+}. Under 254 nm irradiation, the oxide films exhibit bright red, green, and orange emissions for the $(Y_{0.995}Eu_{0.005})_2O_3$, $(Y_{0.97}Tb_{0.03})_2O_3$, and $(Y_{0.965}Eu_{0.005}Tb_{0.03})_2O_3$ films, respectively. The photoluminescence of the oxide films is significantly improved compared with their precursor films, the 613 nm emission intensity of the $(Y_{0.995}Eu_{0.005})_2O_3$ film is nearly 94 times that of LEuH film, while the intensity of 545 nm emission of $(Y_{0.97}Tb_{0.03})_2O_3$ film is about 74 times that of LTbH film. Additionally, the quantum efficiencies of Y_2O_3: RE films were analyzed. Under the 240 nm excitation, the quantum efficiency for $(Y_{0.995}Eu_{0.005})_2O_3$ film is 51.8%, while the quantum efficiency for $(Y_{0.965}Eu_{0.005}Tb_{0.03})_2O_3$ film is 5.8%. Under the 272 nm excitation, the quantum efficiency for $(Y_{0.97}Tb_{0.03})_2O_3$ film is 7.3%.

4. Conclusions

A series of $RE_2(OH)_5NO_3{\cdot}nH_2O$ (RE = La, Pr, Nd, Sm, Eu, Gd, Tb, Dy, Ho and Y) films have been directly prepared via electrodeposition technique within 10 min based on the phase selectivity of LREH and principle of electrodeposition. With this synthetic strategy, the LREH nanosheets were significantly aligned vertically to the substrate surface and showed super-hydrophobicity (with a water contact angle of as high as approximately 150°). The oil/water separator with LYH film coated nickle mesh as functional layers achieved effective separation of petroleum ether and water mixtures based on the super-hydrophobicity. LREH films are crystallized as a low hydration phase (with the d_{002} value of ~8.3–8.9 Å) due to the significant exposure of the hydroxide host layers. The increase in charge density of the hydroxide layer (decrease in RE^{3+} size) alters the spatial orientation of interlayer NO_3^-, making them more perpendicular (less parallel) to the hydroxide layer and increasing the interlayer spacing (d_{002}). The Y_2O_3:RE films, with long luminescence lifetime (1.02-2.09 ms), high quantum efficiency and enhanced luminescence intensity, have been derived from their precursor LYH:RE films via proper annealing at 600 °C for 2 h. The obtained oxide films inherited the morphology of the precursor LYH film and maintained super-hydrophobicity. Significant improvement of photoluminescence of the oxide films have been achieved due to the remove of the quenching groups, $(Y_{0.995}Eu_{0.005})_2O_3$ film exhibited a 613 nm emission intensity 94 times that of LEuH film while $(Y_{0.97}Tb_{0.03})_2O_3$ film exhibits a 545 nm emission intensity about 74 times that of LTbH film. In ternary $(Y_{0.965}Eu_{0.005}Tb_{0.03})_2O_3$ film, the ET from Tb^{3+} to Eu^{3+} was also observed and the efficiency of it was ~51%. The Y_2O_3:RE films exhibited bright emissions with tunable colors (green-orange-red) *via* incorporating different activators.

Author Contributions

Xiaoli Wu: conceptualization, methodology, investigation, validation, data curation, formal analysis, Writing Manuscript. **Yongping Guo**: Formal analysis, validation, data curation. **Ji-Guang Li and Yuanli Liu**: conceptualization, methodology. All authors discussed the results and assisted during manuscript preparation.

Conflicts of interest

We declare that we do not have any commercial or associative interest that represents a conflict of interest in connection with the work submitted.

Acknowledgements

This work was financially supported by the National Natural Science Foundation of China (Grant No. 52062011, 51972047, 51402059) and Natural Science Foundation of Guangxi Zhuang Autonomous Region (No. 2018GXNSFAA050011). We also thank professor L. J. Wang of Guilin University of Technology for providing the measurements of contact angles.

Notes and references

1 F. Gándara, J. Perles, N. Snejko, M. Iglesias, B. Gómez-Lor, E. Gutiérrez-Puebla and M. A. Monge, *Angew. Chem. Int. Ed*., 2006, **118**, 8166-8169.
2 F. X. Geng, Y. Matsushita, R. Z. Ma, H. Xin, M. Tanaka, N. Iyi and T. Sasaki, *Inorg. Chem*., 2009, **48**, 6724-6730.
3 F. X. Geng, R. Z. Ma and T. Sasaki, *Accounts Chem. Res*., 2010, **43**, 1177-1185.
4 X. L. Wu, J.-G. Li, Q. Zhu, W. G. Liu, J. Li, X. D. Li, X. D. Sun and Y. Sakka, *J. Mater. Chem. C*, 2015, **3**, 3428-3437.
5 K.-H. Lee and S.-H. Byeon, *Eur. J. Inorg. Chem*., 2009, 929-936.
6 M. R. Sokolov, Y. Y. Enakieva, A. D. Yapryntsev, A. A. Shiryaev, A. I. Zvyagina and M. A. Kalinina, *Adv. Funct. Mater*., 2020, **30**, 2000681-2000689.
7 F. Gándara, E. Gutiérrez-Puebla, M. Iglesias, D. M. Proserpio, N. Snejko and M. A. Monge, *Chem. Mater*., 2009, **21**, 655-661.
8 Q. Zhu, J.-G. Li, C. Y. Zhi, X. D. Li, X. D. Sun, Y. Sakka, D. Golberg and Y. Bando, *Chem. Mater*., 2010, **22**, 4204-4213.
9 X. L. Wu, J.-G. Li, Q. Zhu, J. K. Li, R. Z. Ma, T. Sasaki, X. D. Li, X. D. Sun and Y. Sakka, *Dalton Trans*., 2012, **41**, 1854-1861.
10 L. Y. Wu, G. M. Chen and Z. B. Li, *Small*, 2017, **13**, 1604070.
11 N. K. Chu, Y. H. Sun, Y. S. Zhao, X. X. Li, G. B. Sun, S. L. Ma and X. J. Yang, *Dalton Trans*., 2012, **41**, 7409-7414.
12 L. L. Liu, M. H. Yu, J. Zhang, B. K. Wang, W. S. Liu and Y. Tang, *J. Mater. Chem. C*, 2015, **3**, 2326-2333.
13 S. H. Liu, J.-G. Li, W. G. Liu, H. Cui, M. M. Liu, J. L. Chen, H. C. Zhu, X. D. Li and X. D. Sun, *Chem. Eng. J*., 2020, **380**, 122618.
14 X. L. Wu, J.-G. Li, J. K. Li, Q. Zhu, X. D. Li, X. D. Sun and Y. Sakka, *Adv. Mater*., 2013, **14**, 015006-015016.
15 X. L. Wu, J.-G. Li, D.-H. Ping, J. K. Li, Q. Zhu, X. D. Li, X. D. Sun and Y. Sakka, *J. Alloys Compd*., 2013, **559**, 188-195.
16 B. Lu, H. M. Cheng, X. X. Xu and H. B. Chen, *J. Am. Ceram. Soc*., 2019, **102**, 118-122.
17 Q. Zhu, S. N. Ding, J. Q. XH, S. Y. Li, X. D. Sun and J.-G. Li, *Chem. Commun*., 2020, **56**, 12761-12764.
18 J. Yao, Q. Zhu and J.-G. Li, *Appl. Surf. Sci*., 2022, **579**, 152226.
19 L. F. Hu, R. Z. Ma, T. C. Ozawa and T. Sasaki, *Angew. Chem., Int. Ed*., 2009, **121**, 3904-3907.
20 Y. S. Yoon, S. H. Byeon and I. S. Lee, *Adv. Mater*., 2010, **22**, 3272-3276.
21 B. I. Lee, E. S. Lee and S. H. Byeon, *Adv. Funct. Mater*., 2012, **22**, 3562-3269.
22 L. F. Hu, R. Z. Ma, T. C. Ozawa and T. Sasaki, *Chem. Asian J*., 2010, **5**, 248-251.
23 Q. Zhu, Z. X. Xu, J.-G. Li, X. D. Li, Y. Qi and X. D. Sun, *Nanoscale Res. Lett*., 2015, **10**, 132.
24 L. F. Hu, R. Z. Ma, T. C. Ozawa, F. X. Geng, N. Iyi and T. Sasaki, *Chem. Commun*., 2008, 4897-4899.
25 Q. Zhu, J.-G. Li, R. Z. Ma, T. Sasaki, X. J. Yang, X. D. Li, X. D. Sun and Y. Sakka, *J. Solid. State. Chem*., 2012, **192**, 229-237.
26 B. Wang and Z. G. Guo, *Chem. Commun*., 2013, **49**, 9416-9418.
27 Z. L. Chu, Y. J. Feng and S. Seeger, *Angew. Chem., Int. Ed*., 2015, **54**, 2328-2338.
28 C. M. Xiao, L. X. Si, Y. M. Liu, G. Q. Guan, D. H. Wu, Z. D. Wang and X. G. Hao, *J. Mater. Chem. A*, 2016, **4**, 8080-8090.
29 N. S. Qu, D. Zhu, K. C. Chan and W. N. Lei, *Surf. Coat. Technol*, 2003, **168**, 123-128.
30 C. Y. Wang, X. Q. Zhang, J. F. Li, X. Y. Qi, Z. Y. Guo, H. Wei and H. B. Chu, *ACS Appl. Mater. Interfaces*, 2021, **13**, 522-530.
31 F. X. Geng, Y. Matsushita, R. Z. Ma, H. Xin, M. Tanaka, F. Izumi, N. Iyi and T. Sasaki, *J. Am. Chem. Soc.*, 2008, **130**, 16344-16350.
32 M. Ogawa and K. Kuroda, *Chem. Rev*., 1995, **95**, 399-438.
33 L. C. Thompson, Complexes, in Handbook on the Physics and Chemistry of Rare Earths, ed. K. A. Gschneidner, Jr. and L. Eyring, North-Holland Physics, Amsterdam, 1979.
34 R. C. Ropp, 1993. (New York: Elsevier)
35 Q. N. Mao, B. Shen, T. Yang, J. S. Zhong and G. Q. Wu, *Ceram. Int.*, 2020, **46**, 19328-19334.
36 C. Y. Cao, H. K. Yang, J. W. Chung, B. K. Moon, B. C. Choi, J. H. Jeong and K. H. Kim, *J. Mater. Chem*., 2011, **21**, 10342-10347.

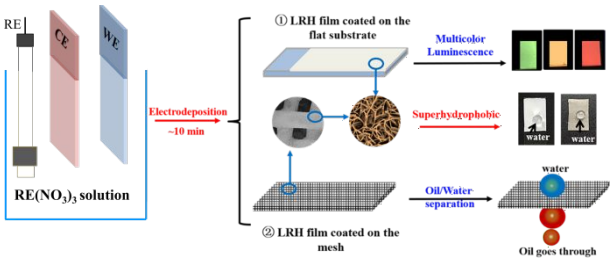

LREH films were prepared on flat substrate and metal mesh via electrodeposition within10 minutes. Y_2O_3: RE films with multicolour luminescence were transformed from the LYH films. In addition, The high efficiency of oil/water separation was achieved with the LYH film grown on a metal mesh.

Fast and Versatile Electrodeposition of vertically Aligned Layered Rare-Earth Hydroxide (LREH) Nanosheets for Multicolor luminescence and Oil/Water Separation

Xiaoli Wu[1,2,3], Yongping Guo[1,2], Ji-Guang Li[4*] and Yuanli Liu[1,2,3*]

1 College of Materials Science and Engineering, Guilin University of Technology, Guilin 541004, P. R. China

2 Guangxi Key Laboratory of Optical and Electronic Materials and Devices, Guilin University of Technology, Guilin 541004, P. R. China

3 Collaborative Innovation Center for Exploration of Hidden Nonferrous Metal Deposits and Development of New Materials in Guangxi; Guilin University of Technology, Guilin 541004, China

4 Advanced Materials Processing Unit, National Institute for Materials Science, Namiki 1-1, Tsukuba, Ibaraki 305-0044, Japan

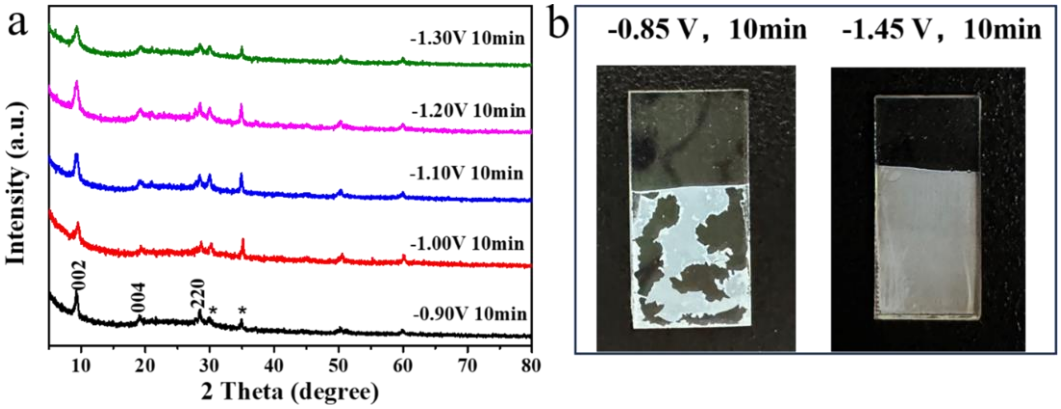

Fig. S1. XRD patterns (a), and actual picture (b) of the $Y_2(OH)_5NO_3 \cdot nH_2O$ film fabricated under different working voltages at room temperature. The peaks marked by asterisks are from the ITO substrate.

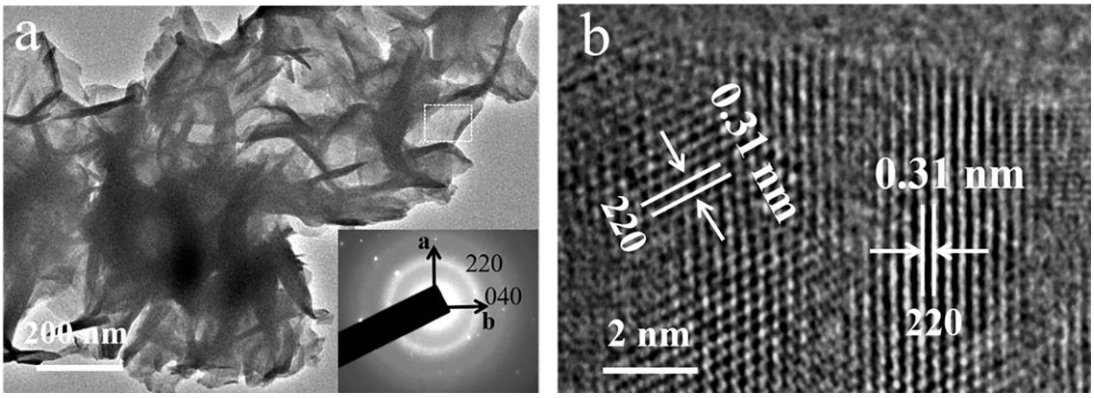

Fig. S2. TEM image (a), and HR-TEM image (b) of the electrodeposited $Y_2(OH)_5NO_3 \cdot nH_2O$ film. The inset in (a) selected area electron diffraction (SAED) taken from the rectangle area.

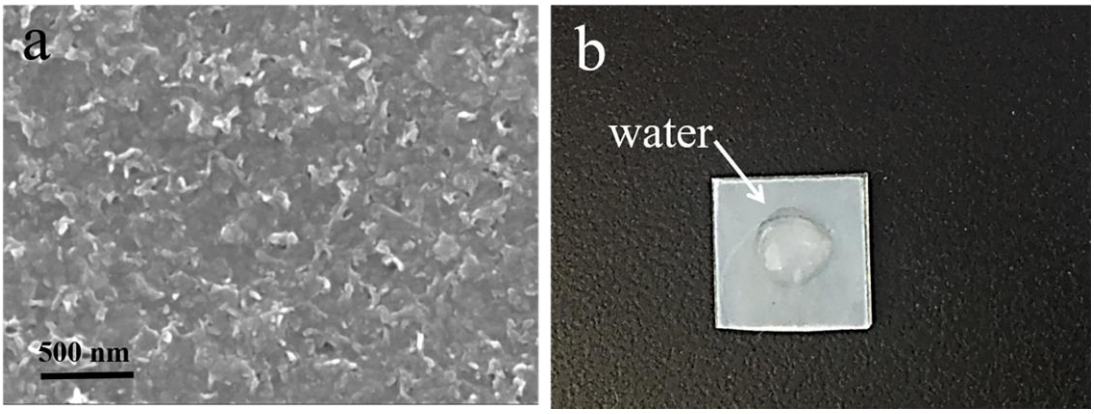

Fig. S3. SEM morphology (a) and the physical image of water droplets attached to the surface (b) of $Y_2(OH)_5NO_3 \cdot nH_2O$ film prepared *via* traditional technique.

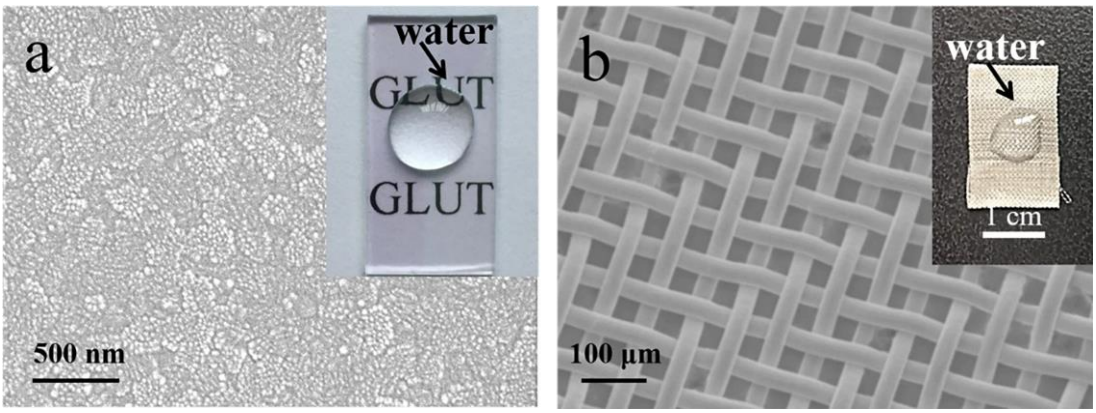

Fig. S4. FE-SEM image of the surface for ITO glass (a) and the original nikle mesh substrate (b). The insets in (a) and (b) are the corresponding physical images of water droplets attached to the surface, respectively.

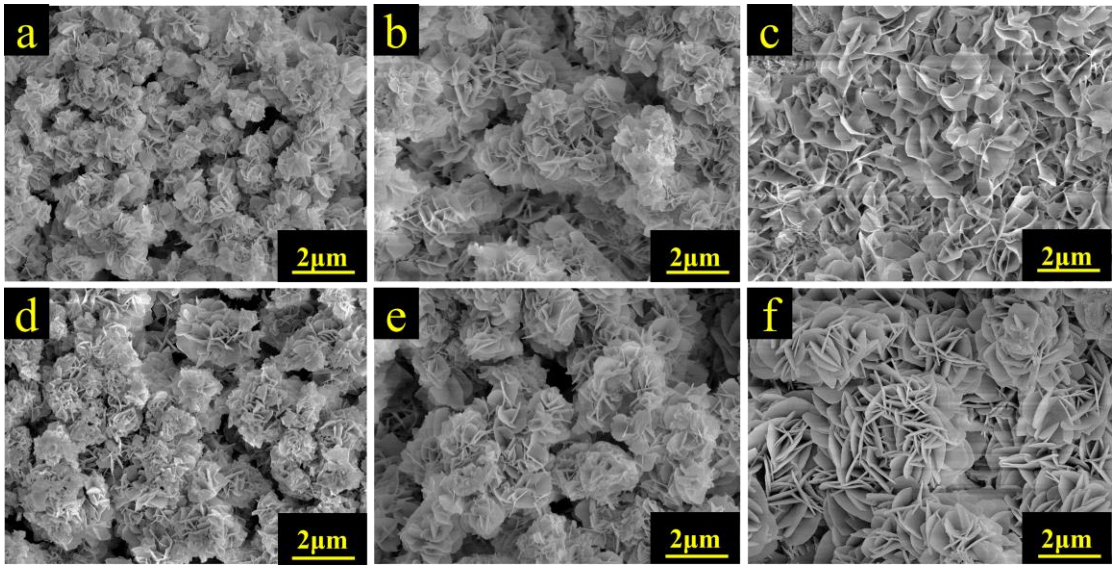

Fig. S5. FE-SEM morphologies of the $Y_2(OH)_5NO_3 \cdot nH_2O$ films fabricated under 40 ºC, -1.10V, 0.1M (a); 40 ºC, -1.20V, 0.1M (b); 40 ºC, -1.30V, 0.1M (c); 30 ºC, -1.10V, 0.1M (a); 55 ºC, -1.10V, 0.1M (b); and 70 ºC, -1.10V, 0.1M (c).

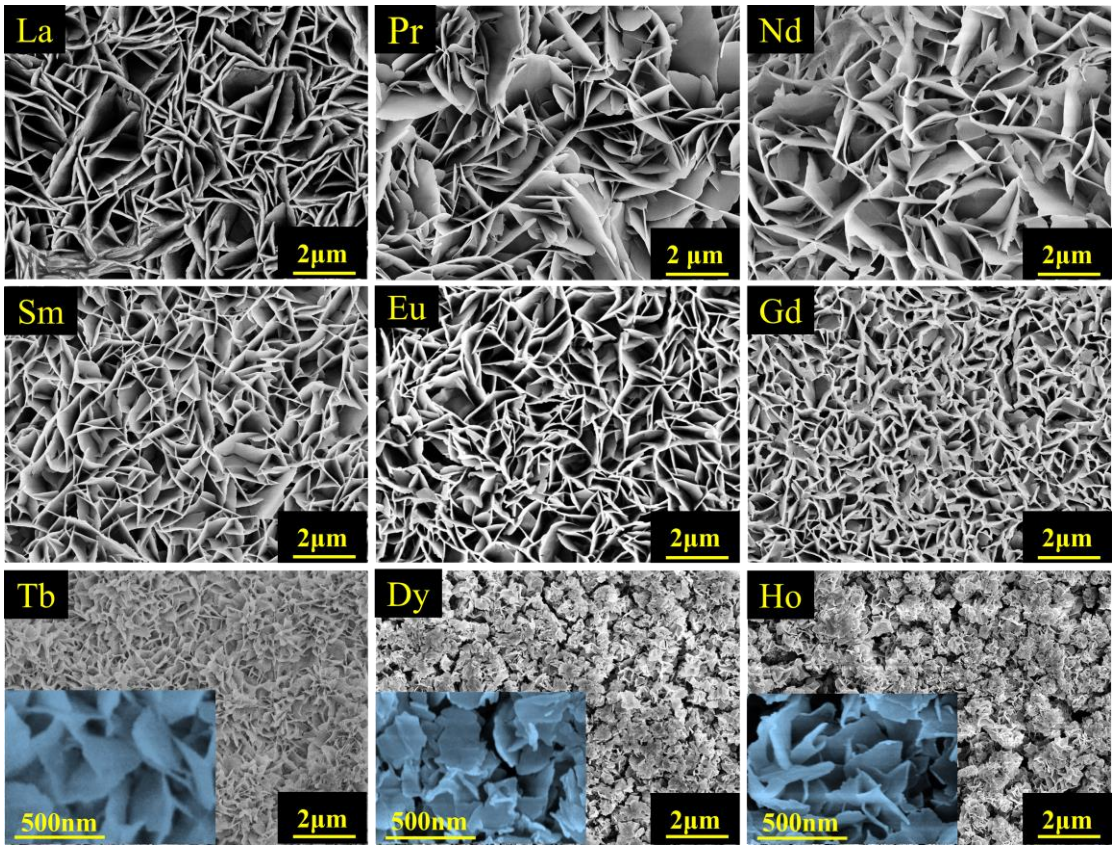

Fig. S6. FE-SEM morphologies of the $RE_2(OH)_5NO_3 \cdot nH_2O$ (RE = La, Pr, Nd, Sm, Eu, Gd, Tb, Dy and Ho) films prepared using 0.1 M $RE(NO_3)_3$ and under the working voltage of -1.15 V at room temperature.

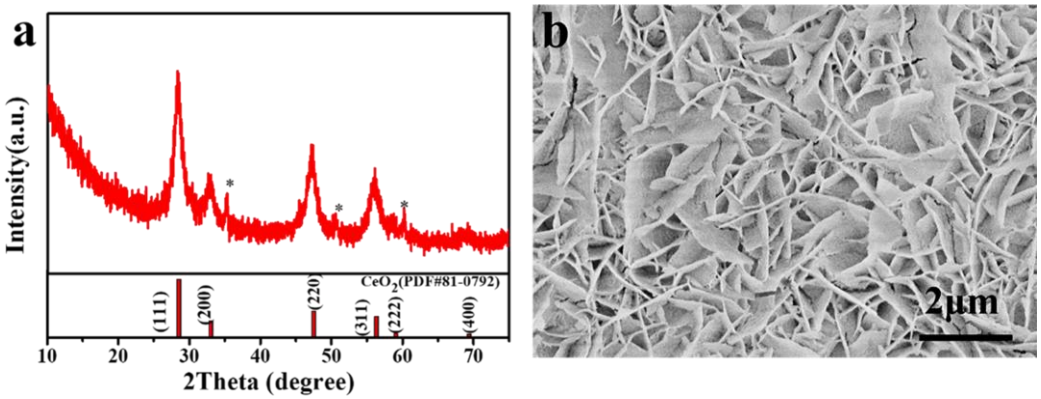

Fig. S7. XRD pattern (a) and FE-SEM observation (b) of the CeO_2 film fabricated using 0.1 M $Ce(NO_3)_3$ and under the working voltage of -1.15 V at room temperature. The peaks marked by asterisks are from the ITO substrate.

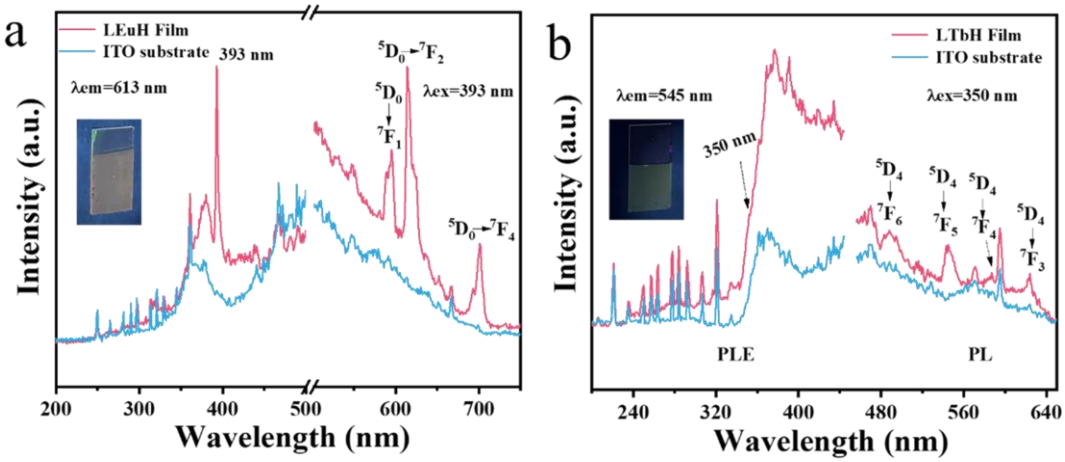

Fig. S8. PL/PLE spectra of the LEuH films under the 393 nm excitation (a); PL/PLE spectra of the LTbH films under the 350 nm excitation (b). The insets of (a-b) show luminescence of the corresponding LEuH/LTbH films under 365 nm excitation from a hand-held UV lamp.